Cohesive laws for shearing of iron/precipitate interfaces

Elzas, A.; Klaver, T. P.C.; Thijsse, B. J.

DOI
10.1016/j.commatsci.2018.03.047

Publication date
2018

Document Version
Accepted author manuscript

Published in
Computational Materials Science

Citation (APA)
Elzas, A., Klaver, T. P. C., & Thijsse, B. J. (2018). Cohesive laws for shearing of iron/precipitate interfaces. *Computational Materials Science*, *152*, 417-429. https://doi.org/10.1016/j.commatsci.2018.03.047

Cohesive laws for shearing of iron/precipitate interfaces

A. Elzas[a,*], T.P.C. Klaver[a], B.J. Thijsse[a]

[a] *Delft University of Technology, Department of Materials Science and Engineering, Mekelweg 2, 2628 CD Delft, The Netherlands*

Abstract

The behaviour of 11 differently oriented iron-precipitate interfaces under a shear load is studied with molecular dynamics simulations. We find that the behaviour depends not only on the interface orientation but also on the shear direction. Furthermore, for many interfaces the presence of a dislocation at the interface triggers a structure change in the interface, and with that completely modifies the shear behaviour. Several interface characteristics are inspected for their possibly decisive influence on the observed loading curves. However, none of these characteristics is found to correlate conclusively with the shear behaviour of the different interfaces. This indicates that actual shear behaviour is rooted in a deeper level of complexity than just depending on the properties of the initial interface. Clearly the time evolution of the interface during shearing is crucial. From the observations a comprehensive cohesive law is derived that represents the shear behaviour for every interface and for both shear directions. This cohesive law can be used in numerical methods at a larger length sale, such as discrete dislocation plasticity.

Keywords: Dislocations, Molecular Dynamics, Shear loading, Iron/precipitate interface, Cohesive law

---

1. Introduction

In everyday use, interfaces in metallic microstructures are routinely subjected to stresses. Deformation and in certain cases mechanical failure are sometimes the ultimate results. Dislocations play an important role in this, but the stress response at interfaces between grains is equally important. Advanced high strength steels show limited ductility due to interface decohesion. To correctly model the material behaviour, so that the limited ductility can be explained, it is crucial to understand the interface behaviour under different loading conditions. This

---

[*] Corresponding author
Email address: `a.elzas@tudelft.nl` (A. Elzas)

Preprint submitted to Elsevier *March 20, 2018*

paper sets out to describe interface behaviour under shear loading, using large-scale atomistic simulations as principal method. Dislocation-interface interactions are part of this study. It will be shown that the same crystals but with different orientations on both sides of the interface give rise to widely different mechanical responses to shear. The ultimate purpose of this paper is not only to identify "weak" interfaces and the reasons therefor, but also to derive from the simulation results cohesive laws, which can be used in numerical methods at the next larger length scales beyond atomic, such as discrete dislocation plasticity where interfaces are modelled by cohesive zone models.

The system under study is Fe – X, with X being a material modelling a hard precipitate. Details are given later. In earlier work [1] we derived tensile traction relations $T_n(u_n)$, where T is traction, u is displacement of two points on opposite sides of the interface and n is the direction normal to the interface. Tensile loading is just one case.

In the present study we use classical molecular dynamics (MD) simulations to derive shear traction relations $T_t(u_t)$, where t is a direction parallel to the interface, for the same 11 interfaces as those studied earlier ($u_n \equiv u_b \equiv 0$, where n is the direction normal to the interface and b is a direction parallel to the interface forming a right-hand coordinate system with n and t). The shear loading is applied in two opposite directions to examine symmetry aspects in the interface behaviour. The simulations are done with and without a dislocation initially present at the interface. The main results of the present work are the cohesive laws that are derived from the observed traction data and a deeper insight in the differences between the various Fe – X interfaces.

Cohesive zone models were introduced by Barenblatt [2] and Dugdale [3], who addressed fracture as a gradual process. They assumed that there is no stress transmission between the fully separated crack surfaces, while a cohesive zone ahead of the crack continues to transmit forces between a pair of virtual surfaces. This behaviour is governed by a traction-crack opening displacement constitutive law.

Cohesive zone models can be either potential-based or non-potential-based. The most commonly implemented cohesive zone model is the potential-based model developed by Xu and Needleman [4]. Here the first derivatives of an interface potential function give the traction-separation relations. The normal and tangential behaviour are coupled, which means that both tractions depend on both the normal and tangential separation. The coupling is controlled by two coupling parameters r and q. The ratio between the work of tangential separation and the work of normal separation, $q = \phi_t/\phi_n$, determines the relative strength of the interface under mode I and mode II separation. The coupling parameter r gives the ratio between the normal separation after complete shear separation without normal traction and a characteristic length for the normal debonding process. Van den Bosch *et al.* [5] have shown that only for $r = q$ the required tangential traction increases with increasing normal compression, as it does in friction. Furthermore, physically realistic coupling is obtained only for $q = 1$, since only then the required normal traction reduces to zero at complete shear separation. However, that implies that $\phi_t = \phi_n$ which experimental studies [6] have shown is often not true. Van den Bosch *et al.* [5] modified the Xu-Needleman cohesive zone model by allowing for $\phi_n \neq \phi_t$. This model is no longer potential-based.

Park *et al.* [7] proposed a potential-based constitutive model where fracture energies are different for the different fracture modes, which they showed is necessary to correctly simulate the mixed-mode fracturing. McGarry *et al.* [8] analysed various cohesive zone models with respect to over-closure and found that when traction-separation relations are obtained from a potential function, non-physical repulsive normal tractions can result when the work of tangential separation exceeds the work of normal separation. They proposed a number of new potential-based and non-potential-based models to control, respectively eliminate, the problem of repulsive normal tractions. Dimitri *et al.* [9] checked various models for their thermodynamical consistency and found that most produce inconsistencies at the local level, which may cause undesirable features in the global behaviour. They also proposed a reformulation of the cohesive zone model by Xu and Needleman [4] as modified by van den Bosch *et al.* [5] within a thermodynamically consistent framework.

Conventionally the parameters for a traction-separation law are obtained empirically, from polycrystalline samples. However, they then reflect the average response of many interfaces. This is therefore inappropriate as a representation of constitutive behaviour of interfacial debonding at the nano-scale. To obtain the parameters of the cohesive law to accurately describe interfacial debonding at the nano-scale atomistic simulations can be used.

Zhou *et al.* [10, 11] derived with MD simulations a cohesive zone law for crack growth at the interface of a brittle material under mixed mode loading. Only one interface was considered. Given the set-up of their simulations, interface sliding and dislocation nucleation and movement were not possible. Spearot *et al.* [12] performed MD simulations on a copper bi-crystal interface under pure shear and pure tensile loading to extract information as input for a cohesive law. In [13] they showed the effect of the deformation path on the resulting microstructure for a nanoscale copper bi-crystal interface. They conclude that 'in order to incorporate path-history dependent effects into continuum interface separation potentials, additional parameters must be used to describe dissipative structural rearrangement within the deformation boundary layer'. Dandekar and Shin [14] parametrised, based on molecular dynamics simulations, a cohesive law for pure mode I and mode II decohesion for an Al-SiC interface. Yamakov *et al.* [15, 16] derived a cohesive zone law from molecular dynamics simulations for implementation in a cohesive zone finite element model for simulating fracture in nano-crystalline or ultrafine grained aluminium. Gupta *et al.* [17] performed MD simulations on an Al(metal)-$Cu_{50}Zr_{50}$(metallic glass) interface under mode I and mode II loading conditions to predict the strength of the interface. Paliwal and Cherkaoui [18] developed for a specific symmetric tilt grain boundary in copper an atomistic simulation based cohesive zone law which accounts for the non-planarity of crack propagation.

Although many studies, as can already be seen in the short selection described above, studied interface behaviour, only little information is available on interfaces in steel. In the present study we therefore examine the behaviour of iron-precipitate interfaces, as a model for the interfaces between the matrix and precipitates that can be encountered in advanced high strength steels. Most of the literature in which cohesive zone law parameters are determined from MD simulations focusses on one particular interface for a certain material (combination). In the present study we derive a cohesive law for 11 different iron-precipitate interfaces under pure shear loading, with and without dislocations interacting with the interface. We show that not just the material combination across the interface, but also the specific orientations of the crystals give a large variety in the response to a shear load. Furthermore, this response is shear direction dependent. Section 2 describes the material, the set-up of the simulations and the analysis methods. The tangential traction relations and the differences in sliding behaviour are described in section 3.1 for simulations without initial dislocations. The role of the geometrical and structural characteristics of the interfaces is studied in section 3.1.4. The influence of an initial dislocation is described in section 3.2. In section 4 cohesive laws are derived which quantitatively describe the relation between T_t and u_t for all interfaces. Finally, conclusions are given in section 5.

2. Method

The response of 11 different iron-precipitate interfaces to a shear load is studied by classical molecular dynamics simulations. The response to a tensile load applied to the same interfaces was already reported in [1]. In the tensile case it was found that stress concentrations may develop which in turn lead to crack nucleation. Here, because of periodic boundaries of the simulation volume, crack nucleation is impossible.

2.1. Material description

Iron is described with the EAM potential by Ackland *et al.* [19]. In the EAM format the potential energy of atom i is given by

$$U_i = F(\rho_i) + 1/2 \sum_j \phi_{ij}(r), \tag{1}$$

where F is the embedding energy of atom Fe or atom X as a function of the local electron density ρ_i, and ϕ_{ij} is the pair interaction between atom i and the surrounding atoms j as a function of their distance r. The local electron density ρ_i is made up from the contributions ψ_j to the electron density by the atoms j surrounding atom i at distances r,

$$\rho_i = \sum_j \psi_j(r). \tag{2}$$

F, ϕ and ψ are relatively simple functions, parametrised for Fe. They can be found in the original paper [19].

The artificial precipitate material X is chosen to be material $X^{(3)}$ from [20]. In this work we choose $\phi_{XX} = 2\phi_{FeFe}$, $a_X = 1.1a_{Fe}$, and the embedding term $F(\rho_i)$ is equal for Fe and X atoms. To create material X with lattice constant $a_X = 1.1a_{Fe}$, we use

$$\begin{aligned} \phi_{XX}(r) &= \phi_{FeFe}(r/1.1), \\ \psi_X(r) &= \psi_{Fe}(r/1.1). \end{aligned} \tag{3}$$

X has thus a 10 % larger lattice constant than Fe and, as a result of the X – X pair interaction being twice as strong as that of Fe – Fe and the X- and Fe-embedding terms being equal, X has a 49 % larger Young's modulus than Fe. Material X is thus stiffer than Fe and, due to the different lattice constant, forms semi- or non-coherent interfaces with Fe. Dislocation transfer into the precipitate material is therefore hindered, just as it is in real precipitate materials found in steel, such as carbides and nitrides of different alloying elements. Similar to [20] the mixed Fe – X pair interaction is a linear combination of the individual Fe – Fe and X – X pair interactions,

$$\phi_{FeX} = q(\phi_{FeFe} + \phi_{XX}), \tag{4}$$

where the factor q in this study equals 1/3. This Fe–X pair interaction in combination with the orientations of the Fe and X grains on either side of the interface determines the interface strength. However, defects at the interface, initially present but also those developing during loading and grain sliding, may be of significant additional influence.

2.2. Setup

The Fe – X system is schematically shown in Figure 1. The system size is dependent on the orientation of the crystals, and on average equals $165 \times 4.4 \times 110$ nm^3, with the number of atoms per system varying between 6 and 9 million. The system is periodic in x and y.

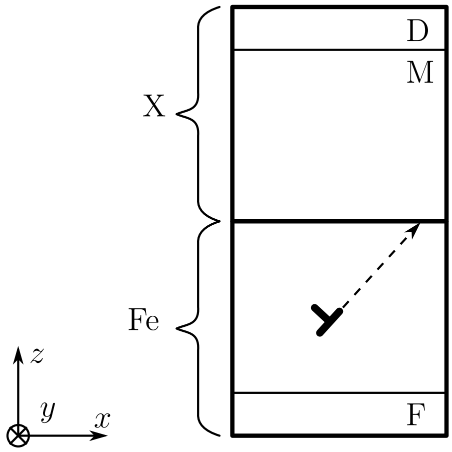

Figure 1: Setup of the simulations. The simulation box consists of an Fe – X bicrystal, which is periodic in x- and y-directions. The atoms in region F are kept fixed, atoms in region M are mobile atoms, whose positions are updated by time integration, and the atoms in region D are moved in the positive or negative x-direction with a constant strain rate of $\dot{\varepsilon} = 10^8$ s^{-1}. In the Fe grain one $\{112\}\langle 111\rangle$ edge dislocation can be inserted close to the interface, so that upon minimisation it moves towards the interface. The X grain is the precipitate material.

The orientations of the 11 different interfaces, being the same as the ones studied in [1], are listed in Table 1. Since in α-iron the typical cleavage plane is the (100) plane, with the crack front direction in either the [001] or the [011] direction, the most logical starting point for the study of interface decohesion, as is also the focus of [1], is a system with the (100) plane at the interface, which upon decohesion becomes the crack plane. To study the interaction of a dislocation with such an interface, the dislocation line has to be in a periodic direction to avoid edge effects. In both [20] and [1] the choice was therefore made to study dislocations of the $\{112\}\langle 111\rangle$ slip system, so that the dislocation line is in the [011] direction, which, with the (100) plane at the interface, is the crack front direction. With this as starting point, the orientations of the iron and precipitate crystal are varied to obtain the orientations given in Table 1. In [1] it was shown that the relation between normal traction T_n and normal separation u_n during crack *growth* is independent of the number of dislocations in the iron grain impinging on the interface. These impinging dislocations cause a stress concentration at the interface, which helps triggering crack *nucleation*. Note that the time needed for crack nucleation does depend on the number of dislocations. In the present study no crack nucleation or decohesion will take place, since only a pure shear load is applied to the system, the system has periodic boundary conditions in the loading direction, and atomic z-displacements are not allowed in regions F and D. The simulations are performed both without dislocations and with one dislocation present in the iron grain at the interface. In this manner not only the pure shear

Table 1: Orientations of the Fe and X grains giving the 11 different interface structures. The angle between the dislocation glide direction and the interface is given as ζ in Fe and η in X.

		Fe			X				
		x	y	z	x	y	z	ζ (°)	η (°)
(100) Fe	S1	$[01\bar{1}]$	$[011]$	$[100]$	$[11\bar{1}]$	$[011]$	$[2\bar{1}1]$	35.3	0.00
	S2	$[01\bar{1}]$	$[011]$	$[100]$	$[01\bar{1}]$	$[011]$	$[100]$	35.3	35.3
	S3	$[01\bar{1}]$	$[011]$	$[100]$	$[\bar{2}3\bar{3}]$	$[011]$	$[31\bar{1}]$	35.3	60.5
	S4	$[01\bar{1}]$	$[011]$	$[100]$	$[21\bar{1}]$	$[011]$	$[1\bar{1}1]$	35.3	90.0
(100) X	Fe1	$[11\bar{1}]$	$[011]$	$[2\bar{1}1]$	$[01\bar{1}]$	$[011]$	$[100]$	0.00[a]	35.3
	Fe3	$[\bar{2}3\bar{3}]$	$[011]$	$[31\bar{1}]$	$[01\bar{1}]$	$[011]$	$[100]$	60.5	35.3
	Fe4	$[21\bar{1}]$	$[011]$	$[1\bar{1}1]$	$[01\bar{1}]$	$[011]$	$[100]$	90.0[b]	35.3
(110) Fe	X1	$[001]$	$[1\bar{1}0]$	$[110]$	$[111]$	$[1\bar{1}0]$	$[11\bar{2}]$	54.7	0.00
	X2	$[001]$	$[1\bar{1}0]$	$[110]$	$[113]$	$[1\bar{1}0]$	$[33\bar{2}]$	54.7	29.5
	X3	$[001]$	$[1\bar{1}0]$	$[110]$	$[001]$	$[1\bar{1}0]$	$[110]$	54.7	54.7
	X4	$[001]$	$[1\bar{1}0]$	$[110]$	$[\bar{1}\bar{1}2]$	$[1\bar{1}0]$	$[111]$	54.7	90.0

[a] The dislocation is placed in the $[1\bar{1}1]$ direction, giving an angle between slip plane and crack plane of 70.6°.

[b] The dislocation is placed in the $[\bar{1}\bar{1}1]$ direction, giving an angle between slip plane and crack plane of 19.4°.

behaviour but also the influence of a dislocation can be studied. The dislocation is initially placed in the iron grain at 10 Å underneath the interface by removing a half plane of atoms. Upon energy minimisation the dislocation moves to the interface where it halts. By starting the simulations with the dislocation at the interface, instead of far below the interface, the influence of the different angles between glide plane and loading direction for the different oriented Fe grains is minimised.

In the simulations, atoms in the lower 10 Å are kept fixed, region F in Figure 1. On atoms in the upper 10 Å, region D, a tangential displacement is imposed with a constant strain rate $\dot{\varepsilon}$ of 10^8 s^{-1}. For the mobile atoms, region M, time integration using a time step of 5 fs is performed at 1 K with a Nosé-Hoover thermostat. Prior to loading, the system is equilibrated at 1 K for 100 ps. The stress σ that results from the applied strain is calculated by summing the resulting forces on the atoms in region D and dividing this by the area in the x, y-plane.

The very low temperature of 1 K was chosen to be able to see details of the atomic behaviour driving the interface dynamics. At higher temperatures these details would be hidden by thermal vibrations.

The particular interface realisations for each of the 11 crystal orientations are taken from [1], where they were created using the method described by Tschopp and McDowell [21]. A systematic collection of interface structures was generated by energy minimisation following extremely small initial displacements in the x and y directions. Of all the possible interface structures thus generated, the structure of which the interface energy has the highest number of occurrences in the collection is chosen as the final realisation.

2.3. Local behaviour

Similar to [1], to calculate the local response to the applied load in the interface region, the region is divided into multiple bins along the x-direction. Each bin is then divided in two: one half above the interface, one half underneath, as shown in Figure 2. The width of each bin, δx, was chosen to be 8.8 Å, or five atomic [100] planes. The height of the bins, δz, was chosen as 20 Å. This ensures that the total interface region, which is the region in which significant extra strain is seen with respect to the bulk, is taken into account in the calculations made over each bin.

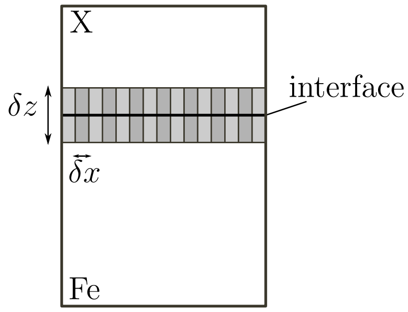

Figure 2: Division of interface region into bins with width δx of 8.8 Å and height δz of 20 Å. The bins have a role only in the data analysis, not in the simulation.

For every bin i the stress is calculated as the average of the stresses on the N_i atoms j in the bin, according to

$$\sigma_i = \frac{1}{N_i} \sum_{j=1}^{N_i} \sigma_{ij}. \tag{5}$$

The tangential traction T_t in a bin is equal to the xz component of this average stress in the bin.

The tangential separation u_t between the bins above and underneath the interface is calculated as the tangential distance between the centers of mass (c) of these bins

$$u_t = x_{\rm c}^{X} - x_{\rm c}^{Fe}, \tag{6}$$

where x_{c}^{Fe} is the x-position of the center of mass of the Fe-bin (below the interface) and x_{c}^{X} is the x-position of the X-bin, above the interface. For simplicity of notation, T_t and u_t do not carry a subscript designating the bin to which they apply. The values for T_t and u_t were calculated every 100 time steps (500 fs) as an average over 10 time steps (50 fs).

To determine T_n and u_n in [1], the allocation of atoms to bins was made every time step when these values were calculated. To determine T_t and u_t in this study, the allocation to bins is made once, at the beginning of the simulation. This difference is necessary since interface sliding occurs under shear loading. To determine the tangential displacement, the displacements with respect to the original positions need to be used.

In addition to the $T_t(u_t)$ results for individual bins, the data are also averaged over the entire interface and over time intervals of 10 ps. This averaging is done to smoothen the curves and get a better view on the similarities and differences between the different interfaces and loading directions. These average traction data are indicated as $\overline{T_t}(u_t)$. Also, in isolated cases, the standard deviation of these data points $S(T_t(u_t))$ is reported. This quantity reflects the homogeneity of the traction value along the interface.

2.4. Methods

The MD-simulations are performed with LAMMPS [22, 23] and the GPU-accelerated version hereof [24, 25, 26]. The structures are visualised with OVITO [27]. As a measure for changes in the interface structure the number of non-bcc atoms at the interface is determined with the common neighbour analysis as implemented in LAMMPS [28, 29]. We found this to be a sensitive diagnostic for recording structural changes at an interface.

3. Results

In the following we present the results of this work. Section 3.1 shows that without dislocations present the interfaces can be divided in three different categories: those that show equal behaviour under opposite shearing direction, Section 3.1.1, those that show a small difference in behaviour under opposite shearing directions, Section 3.1.2, and those that show a large difference in behaviour under opposite shearing directions, Section 3.1.3. Section 3.1.4 discusses the characteristics of the different interfaces and their relation, or the absence of a relation, with the behaviour of the interfaces under a shear load. With an initial dislocation present at the interface, the interfaces can be divided in two categories : those where the dislocation does not influence the behaviour under a shear load, Section 3.2.1, and those where the dislocation changes the interface structure and with that the behaviour under a shear load, Sections 3.2.2 and 3.2.3. The influence of the dislocation slip plane and the loading direction is discussed in Section 3.2.4.

As a reference to the 11 different Fe − X bicrystal interfaces, of which the crystallographic data were given in Table 1, we show the initial atomic structures in Figure 3 and those after 500 ps shear loading in positive x-direction in Figure 4.

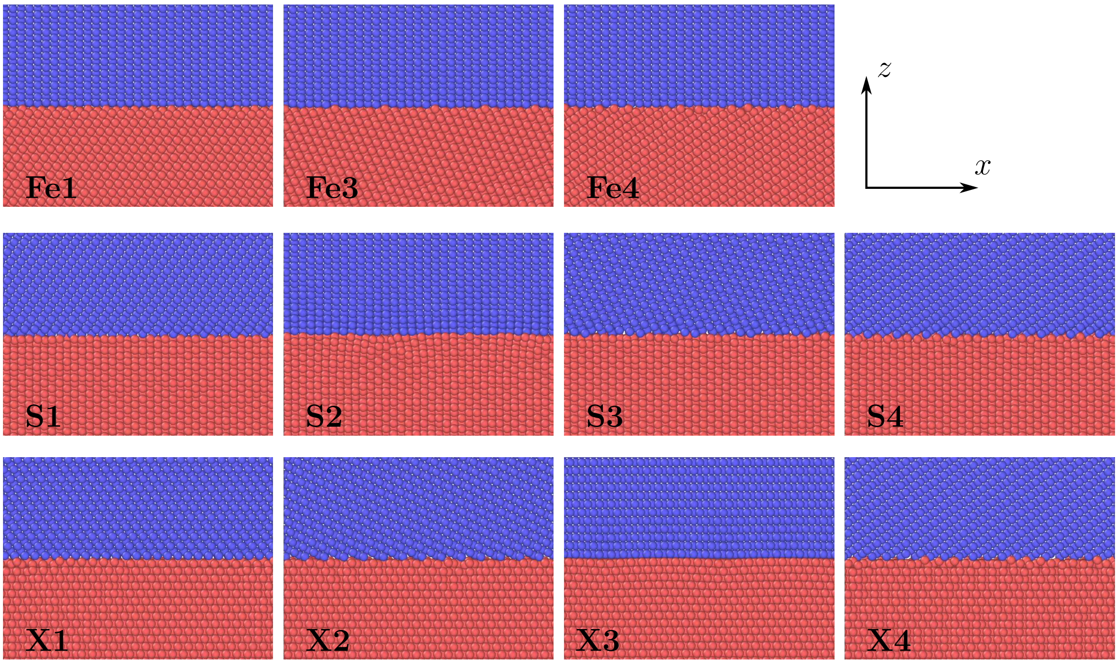

Figure 3: Atomic positions at the interfaces. Atoms in blue are X, atoms in red are Fe.

3.1. Shear loading without dislocations

For all interfaces and loading directions the upper crystal eventually slides over the lower crystal. Yet, the system responses vary. For some interfaces the tangential traction versus tangential separation ($T_t(u_t)$) for all bins follows a very similar periodic behaviour, as illustrated in Figure 5a for the X1 interface, where the traction behaviour is shown for five different bins, indicated by their initial x-positions x_0 (for clearer visibility the curves for the different bins have been shifted along the T_t-axis). For some other interfaces, however, first a barrier needs to be overcome in every bin before sliding starts, as is shown by a non-zero value (roughly 3 GPa) of the sliding resistance T_t^s. This is illustrated for five bins of the Fe4 interface in Figure 5b.

As can be seen in Figure 5a, for all the bins along the X1 interface the behaviour is similar. For the Fe4 interface the behaviour of the individual bins is dissimilar,

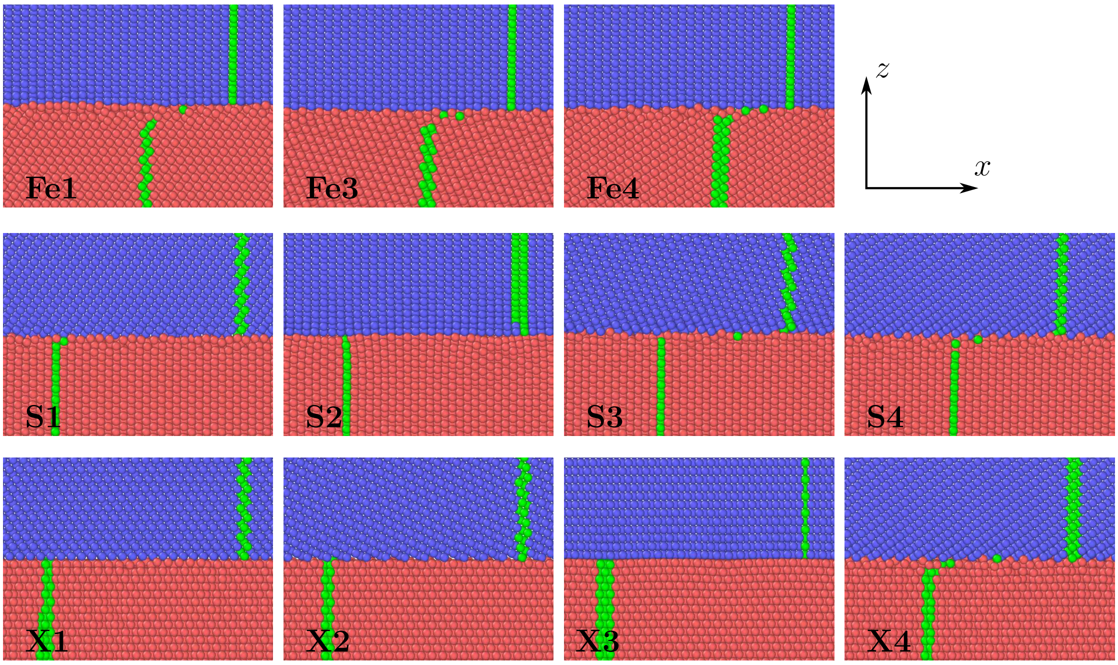

Figure 4: Atomic positions at the interfaces after 500 ps of shearing in the positive x-direction. Atoms in blue are X, atoms in red are Fe. Atoms marked in green formed one vertical plane before shearing.

more chaotic and not as clearly periodic as for the X1 interface (5b). It is therefore harder to notice common patterns in the different bins. However, the averages and the standard deviations over time of the tangential traction during sliding are equal for the different bins, which does show a certain similarity between the bins. Therefore, for easy comparison, for every interface and loading direction the average $\overline{T_t}$ over the bins is determined. Also, the interface structures are analysed. As mentioned above, three different kinds of behaviour are seen for the 11 interfaces: 1. equal behaviour for shearing in opposite directions, 2. slightly different behaviour for shearing in opposite directions, 3. very different behaviour for shearing in opposite directions. We will next discuss these different types.

3.1.1. Equal behaviour for shearing in opposite directions

For the S2, X1 and X3 systems the average tangential tractions $\overline{T_t}(u_t)$ are equal for shearing in opposite directions, see Figures 6 and 7 (X1 is similar to X3). These interfaces all have a structure that is quite flat and is mirror symmetric along the $y-z$ plane, Figure 3. Therefore it is not surprising that the behaviour is the same in both shearing directions. Because of the flatness of the Fe and X surfaces at the interface, these Fe and X crystals clearly slide along the interface as rigid blocks, and not, as is seen for most of the other interfaces, following a gradual slip profile

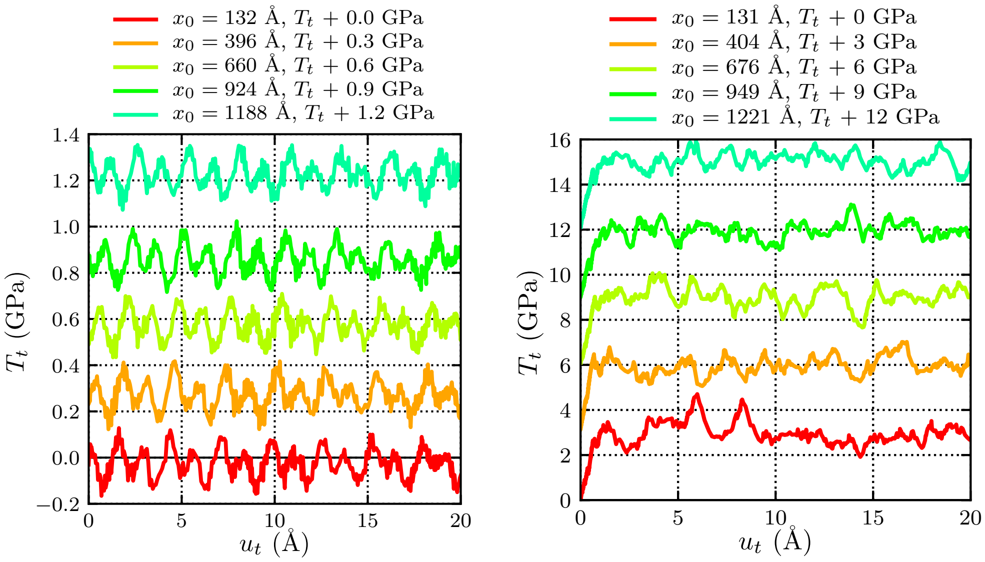

(a) X1

(b) Fe4

Figure 5: Two examples of different sliding behaviour at different interfaces. Tangential traction versus tangential separation for five bins along the X1 and Fe4 interfaces under shearing in the positive x-direction. For a clearer view on the behaviour of individual bins the curves have been shifted vertically. The initial bin positions are indicated by x_0. Note the difference in vertical scale for the two interfaces.

of the top Fe planes, Figure 4.

This can be further quantified by looking at the structure of the interface. As a measure for changes in the interface structure we record the number of non-bcc atoms per unit of interface area, n_{int}. This number hardly changes for S2 (Figure 7(bottom)), X1 and X3 (Figure 6(bottom)), and one can therefore conclude that the interface structure does not change, which again indicates that the sliding takes place as rigid crystal blocks along these interfaces. The sliding along the X3 interface, Figure 6(top), and along the X1 interface (not shown) takes place at near-zero resistance. For S2 a barrier in $\overline{T_t}(u_t)$ has to be overcome before the crystals start sliding, as shown by the non-zero steady-state resistance, Figure 7.

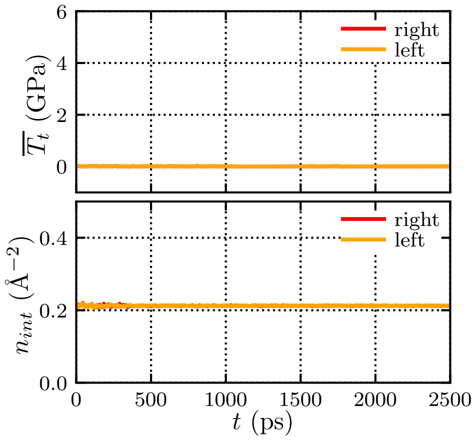

Figure 6: Time evolution of tangential traction averaged over all bins along the interface (top) and number of non-bcc atoms per unit interface area (bottom) for the X3 interface (see Figure 3) under shear loading in opposite directions. To smoothen the curves the data points are averaged over 10 ps.

3.1.2. Small difference between shearing in opposite directions

The Fe1, Fe3, Fe4, S1, S3, and S4 interfaces show small differences for shearing in opposite directions. This is caused by the initial interface structures, Figure 3, having deviations from mirror-symmetry. After 500 ps of shearing, Figure 4, all these interfaces show sliding of the X crystal with respect to the Fe crystal in another way than sliding as rigid blocks. The upper atomic Fe layers exhibit a gradual slip profile in the shearing direction, as can be seen by the displacement of the atoms marked in green.

During shearing and before sliding, the tangential traction increases and the number of non-bcc Fe and X atoms changes, as is illustrated in Figure 8 for the Fe4 interface. Once the upper crystal slides with respect to the lower crystal, the structure of the interface no longer changes, as is indicated by the constant n_{int},

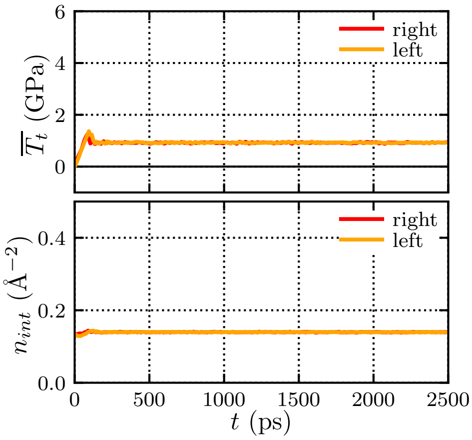

Figure 7: Time evolution of tangential traction averaged over all bins along the interface (top) and number of non-bcc atoms per unit interface area (bottom) for the S2 interface (see Figure 3) under shear loading in opposite directions. To smoothen the curves the data points are averaged over 10 ps.

and the tangential traction becomes constant: a steady-state sliding behaviour develops. We find a small difference between the responses to shearing in the two directions. The barrier which needs to be overcome to start sliding is higher when shearing to the left, which is reflected by a small peak in the tangential traction and a different change in interface structure compared to shearing to the right.

The Fe1, S1, S3, and S4 interfaces show a similar behaviour as the Fe4 interface, i.e. with only a small difference between shearing to the left or to the right. The Fe3 interface shows a slightly different behaviour, which is explained in Appendix A.

3.1.3. Large difference for shearing in opposite directions

For the X2 and X4 interfaces, due to their saw tooth structure as shown in Figure 3, there are large differences between shearing in opposite directions. In one direction sliding takes place almost without resistance, while in the other a barrier has to be overcome, and sliding occurs with a resistance of almost 2 GPa. Figure 9 illustrates this behaviour for the X2 interface. Shearing to the right leads to sliding at near zero friction, without a change in interface structure, as indicated by the constant number of non-bcc atoms. As can be seen in Figure 4, this sliding occurs as rigid blocks. When sheared to the left, a barrier has to be overcome and the structure slides at a tangential traction of almost 2 GPa while the interface structure changes. In this case, atoms in the upper Fe planes follow a gradual slip profile in the shearing direction. Conversely, the X4 crystals show the same behaviour but in opposite direction.

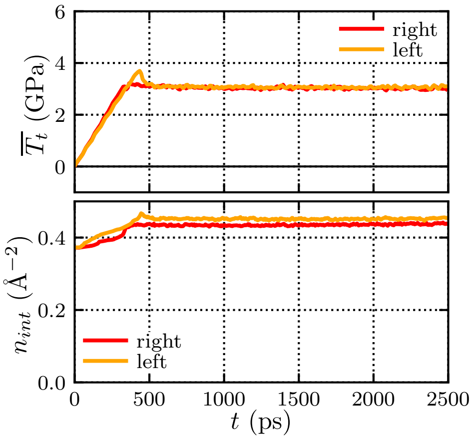

Figure 8: Time evolution of tangential traction averaged over all bins along the interface (top) and number of non-bcc atoms per unit interface area (bottom) for the Fe4 interface (see Figure 3) under shear loading in opposite directions. To smoothen the curves the data points are averaged over 10 ps.

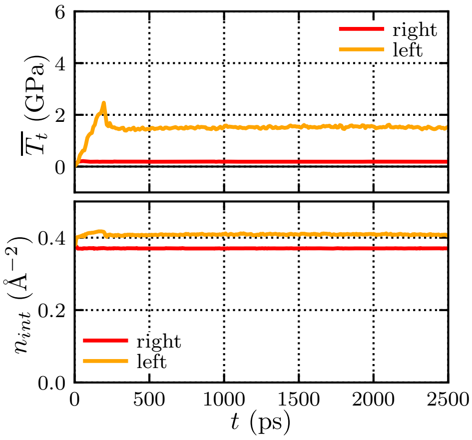

Figure 9: Time evolution of tangential traction averaged over all bins along the interface (top) and number of non-bcc atoms per unit interface area (bottom) for the X2 interface (see Figure 3) under shear loading in opposite directions. To smoothen the curves the data points are averaged over 10 ps.

3.1.4. Interface characteristics

To understand the different sliding behaviours of the different interfaces, we need to study the interfaces in more detail. They can be characterised by the orientations of the crystals on either side, but this alone does not specify the interface completely, as the precise geometrical structure and the energy play additional roles. In this section we will therefore describe first the energy of the interface and its relation with the sliding behaviour and then the geometrical structure and its relation with sliding.

As explained in Section 2.2, for every orientation the particular interface realisation studied has a structure of which the energy has the highest number of occurrences among all realisations studied. Only for the S2, X1 and X3 systems this energy is equal to the minimum interface energy for these particular orientations, and only these three systems slide as rigid blocks in both shearing directions. A possible reason for this is that during sliding, systems for which the minimum interface energy is the most occurring interface energy can move from one lowest-energy configuration to the next, whereas this is not possible for the other systems. The value of the interface energy itself shows no relation with the resistance of the interface to sliding. We find that for systems with one common crystal orientation, however, a lower interface energy does give a higher resistance to sliding and therefore a higher T_t^s.

The geometrical structure of the interface can be described in terms of the atomic density, the number of non-bcc atoms, the minimum distance between Fe and X atoms at the interface, and the degree of intermixing of Fe and X at the interface. No relation is found between the atomic density at the interface and T_t^s. A general relation (valid for all interfaces) between any of the other three terms and the sliding resistance is not found either. However, for systems with one common crystal orientation, certain correlations are found. For these systems (1) a higher number of non-bcc Fe atoms at the interface gives a higher T_t^s. The number of non-bcc X atoms does not play a role in determining the sliding resistance, since X is stiffer than Fe and therefore only Fe, and not X, atoms follow a gradual slip profile in the shearing direction. The number of non-bcc X atoms is therefore not a factor determining the sliding resistance. (2) A smaller distance between Fe and X atoms at the interface gives a higher sliding resistance, as does (3) an increased level of intermixing at the interface.

3.2. Shear loading with dislocation

With one dislocation initially present in the iron grain at the interface the systems are again subjected to shear loads in opposite directions to investigate how the dislocation influences the behaviour of the interfaces. Three different kinds of influence are observed: 1. No influence, 2. A large influence under both shearing directions, 3. An influence for shearing in one direction only.

3.2.1. No influence of dislocation

The overall interface behaviour without a dislocation is not changed by the presence of a dislocation for the Fe1, Fe3, Fe4, S1, S3, S4, and X4 interfaces. The initial stress profile along the interface is locally influenced by the presence of a dislocation, as illustrated in Figure 10 for the Fe4 interface and in Figure 11 for the X4 interface. After 2500 ps of shearing we find two different types of behaviour. Either the dislocation can no longer be distinguished in the stress profile because it has dissolved in the interface, and the interface behaviour is not modified (Figure 10), or the dislocation can still be clearly distinguished, since the stress profile is only locally modified, just as it was initially. The behaviour along the rest of the interface, however, is not modified, as illustrated in Figure 11.

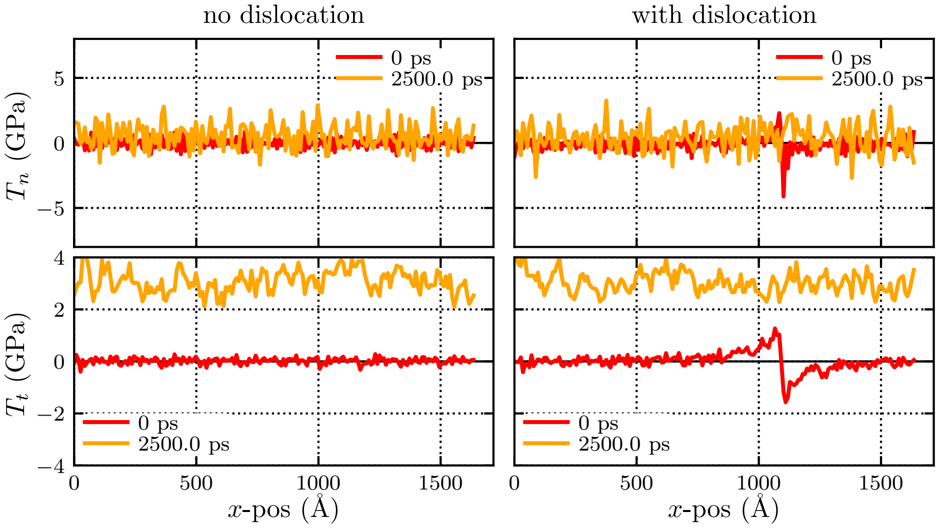

Figure 10: Initial and final (after 2500 ps shear in the negative x-direction) normal and tangential traction profiles along the Fe4 interface with and without an initial dislocation.

3.2.2. Large influence of dislocation in both directions

As can be seen when comparing Figures 7 and 12, an initial dislocation at the S2 interface has a large but unequal influence on the shearing behaviour in both directions. Initially this interface has a regular structure of misfit dislocations, in which the initial dislocation in the iron crystal can be clearly distinguished (Figure 13, top). When a shear load in positive x-direction is applied to the system, the interface structure starts to change from this dislocation onward in both directions along the interface. After 900 ps of shear loading, the structure change has reached bin 60 (about 300 Å to the right of the initial dislocation position), as shown in Figure 13, bottom. This change in structure is accompanied by a change in the

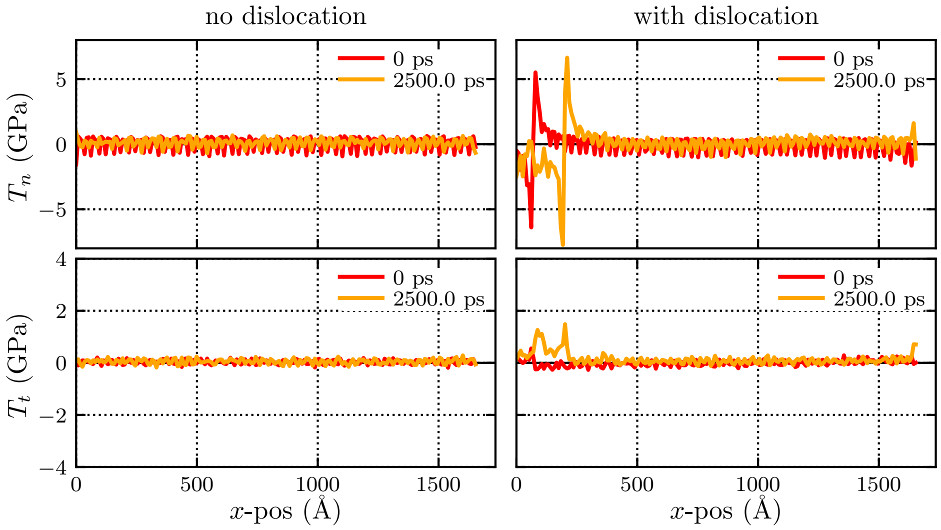

Figure 11: Initial and final (after 2500 ps shear in the negative x-direction) normal and tangential traction profiles along the X4 interface with and without an initial dislocation.

tangential traction, as can be seen in Figure 14, where the tangential traction is shown versus time at different positions along the interface. Since in Figure 12 averages over the interface are shown, the graphs in this figure show a gradual increase. Although the S2 interface is symmetric along the z-axis, the dislocation placed in the iron crystal has a slip plane at an angle with this axis, and therefore the symmetry is broken and the structure change, and with that the observed traction, is different under different loading directions.

3.2.3. Influence of dislocation in one direction only

The behaviour of the X1, X2, and X3 interfaces only changes by an initial dislocation when sheared to the right. Without a dislocation shearing to the right leads to interface sliding at a near-zero tangential traction and without a change of interface structure, as illustrated in Figure 6 for the X3 interface. With a dislocation, as illustrated in Figure 15, the structure still starts sliding at a very low traction, but once the structure slides the mean tangential traction and the size of its oscillations gradually increase and the number of non-bcc atoms at the interface changes. Similar as for the S2 interface a gradual structure change along the interface from the dislocation position on explains this behaviour.

3.2.4. Influence of slip plane and loading direction

From the previous sections we can conclude that a dislocation only influences the response during shearing when the crystals, without a dislocation, slide as rigid blocks, so without a structure change at the interface. Only when the dislocation

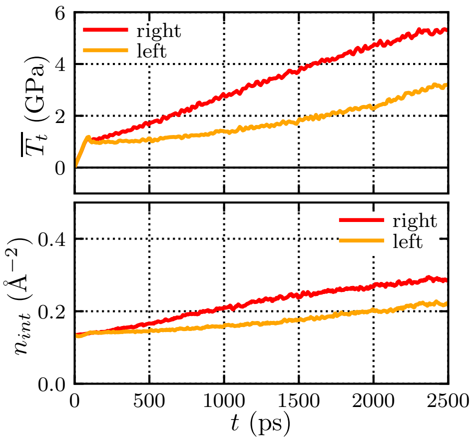

Figure 12: Time evolution of tangential traction averaged over all bins along the interface (top) and number of non-bcc atoms per unit interface area (bottom) for the S2 interface (see Figure 3) with one initial dislocation in the Fe crystal, under shear loading in opposite directions. To smoothen the curves the data points are averaged over 10 ps.

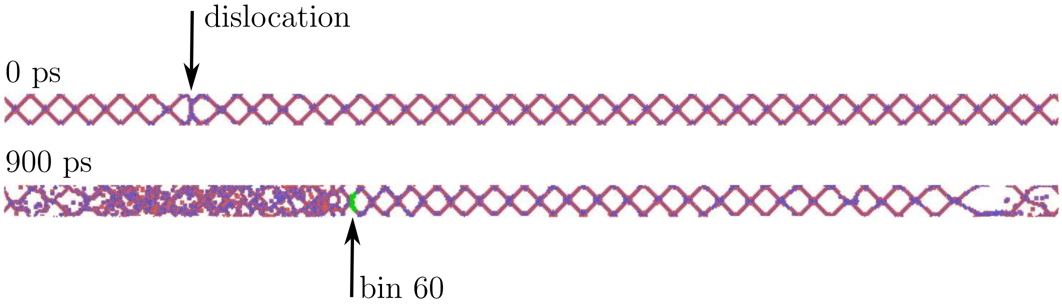

Figure 13: Top view of the non-bcc atoms in the S2-interface before (top) and after 900 ps of tangential loading (bottom). In the top figure the dislocation can be clearly distinguished in the interface. In the bottom figure, after 900 ps, the atoms in bin 60 are marked in green, and the interface structure to the left of this bin has undergone a change, which is accompanied by an increase in tangential traction (shown in Figure 14).

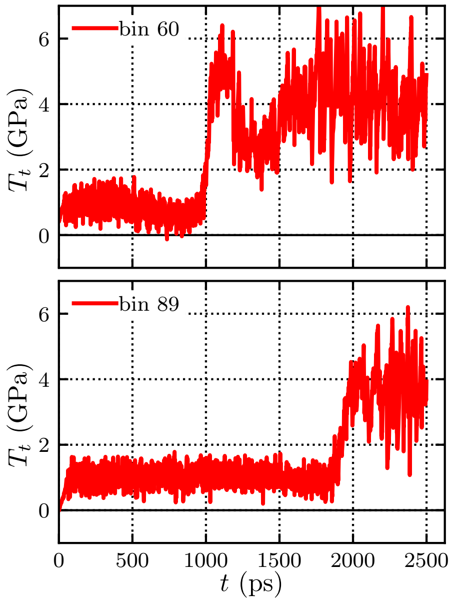

Figure 14: Tangential traction versus time at two different positions (bins) along the S2-interface under shear loading.

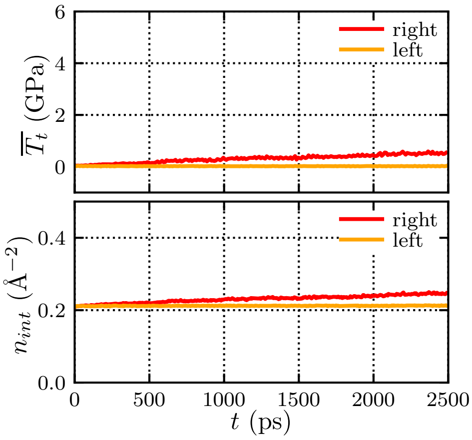

Figure 15: Time evolution of tangential traction averaged over all bins along the interface (top) and number of non-bcc atoms per unit interface area (bottom) for the X3 interface (see Figure 3) with one initial dislocation in the Fe crystal, under shear loading in opposite directions. To smoothen the curves the data points are averaged over 10 ps.

triggers a structure change, the response of the system is modified. This can depend on the loading direction, and therefore on the resolved shear stress on the dislocation, as seen for the X1 and X3 interface for which the shear behaviour is modified by the presence of a dislocation only when sheared in the positive x-direction.

When the crystals slide along the interfaces by an atomic slip profile of the upper Fe planes with some changes in the interface structure, the interface can accommodate the dislocation, either by letting it dissolve in the interface or leaving it in the interface unmodified, and its presence does not influence the response along the interface outside the region where the dislocation is accommodated.

As shown in the previous sections a structure change of the interface leads to a different interface behaviour. The loading direction, the interface, and the dislocation all determine the structure change. A different structure change leads to a different interface behaviour.

4. Cohesive law

Subjecting the 11 different interfaces to a shear load shows that the relation between tangential traction T_t and tangential separation u_t is not only interface dependent. It also depends on the shearing direction. Furthermore, the relation can be modified by impinging dislocations. A cohesive law giving the relation between tangential traction and separation should therefore capture all these effects.

We find from the simulation results that, without dislocations present, the relation between T_t and u_t can be described in three parts (Figure 16): an elastic part for separations smaller than the critical separation u_t^{crit}, a steady-state sliding part for separations larger than u_t^s and a quadratic part in between, where the steady-state sliding behaviour develops:

$$\begin{aligned}
T_t &= \frac{T_t^{crit}}{u_t^{crit}} u_t, && \text{for } 0 \leqslant u_t \leqslant u_t^{crit},\\
T_t &= \frac{T_t^{crit} - T_t^s}{(u_t^s - u_t^{crit})^2}(u_t - u_t^s)^2 + T_t^s, && \text{for } u_t^{crit} \leqslant u_t \leqslant u_t^s,\\
T_t &= T_t^s, && \text{for } u_t \geqslant u_t^s.
\end{aligned} \tag{7}$$

Here u_t^{crit} is the separation at which the structure starts to slide, T_t^{crit} is the corresponding value of the traction, u_t^s is the separation at which steady-state sliding behaviour is reached, and T_t^s is the corresponding sliding traction. For shearing in the negative x-direction the same relation is found, with negative values for the tractions and separations. Figure 17 shows the obtained results for three of the interfaces. In Table B.2 in Appendix B the parameters for the cohesive

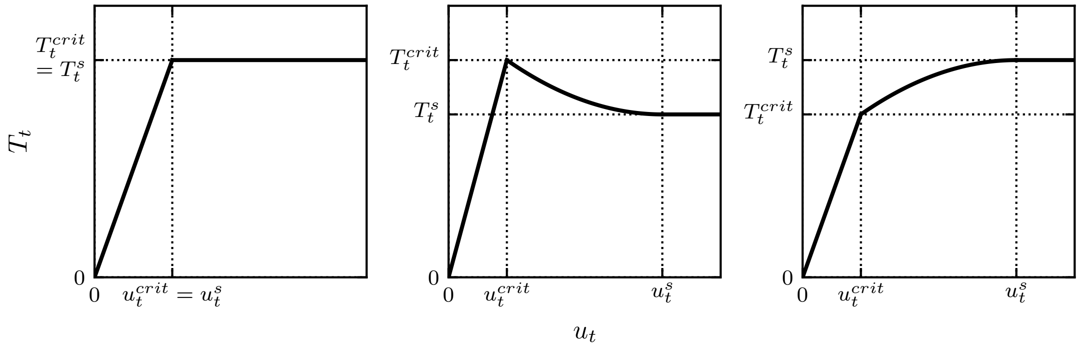

Figure 16: Three possible shapes of the cohesive law (Equation 7) describing the relation between T_t and u_t.

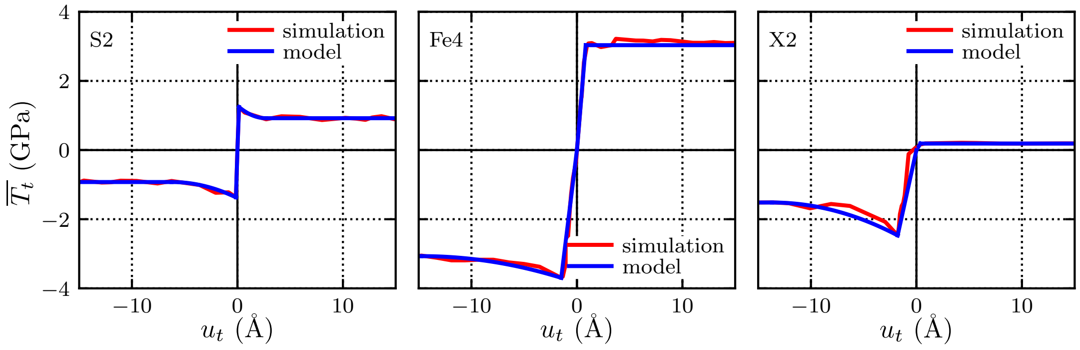

Figure 17: T_t versus u_t for three interfaces as obtained from the simulations and as expressed by the fitted cohesive law, Equation 7, with the parameters given in Table B.2

law are given for all the interfaces and for both shearing directions. This is one of the principal results of this work.

With dislocations present, as was shown in Section 3.2, it is found that for several interfaces the structure of the interface changes upon sliding, which results in a changed relation between traction and separation. When this happens, the structure changes gradually outward from the dislocation position, not unlike the fronts of a phase transition. During shearing there will be a part of the interface which still has the original structure A_{orig} and a part which has a new structure A_{new}. The fraction ξ of changed interface area can be used as a running parameter representing the progress of the "phase transition",

$$\xi = \frac{A_{new}}{A_{orig} + A_{new}}. \tag{8}$$

In our current model it is assumed that for the unchanged part of the interface the original cohesive law T_t derived without a dislocation is still valid. For the changed part of the interface a different relation between T_t and u_t exists, T_t^{new}. The overall cohesive law for the changing interface is then given by

$$T_t = (1-\xi)T_t^{orig} + \xi T_t^{new}, \tag{9}$$

where T_t^{orig} is now used for the original cohesive law T_t of Equation 7. For those interfaces where the structure changes by the presence of a dislocation, the boundaries between the changed and unchanged parts of the interface are determined by analysing the number of non-bcc Fe and X atoms in every bin along the interface, since this number changes when the structure changes. The time dependence then yields the rate of structure change $\dot{A}_{new}$. Upon sliding, the initial positions of the dislocation in the upper and lower crystal move apart, as is schematically illustrated in Figure 18. When initially the structure of both the Fe and the X crystal is locally modified at the initial position of the dislocation, one can imagine that when these two locally modified parts move apart, the structure of the region in between will also change. As is shown in Figure 18, the part of the interface with the new structure, A_{new}, would be then the part in between the initial dislocation positions in Fe and X and the rest of the interface, A_{orig}, would stil have the original structure. $\dot{A}_{new}$ would then be equal to the sliding velocity, which is determined by $\dot{\varepsilon}$.

However, the rate of structure change $\dot{A}_{new}$ is always larger than the sliding velocity, which is 110 Å/ns for $\dot{\varepsilon} = 10^8\text{s}^{-1}$. This is shown in Figure 19, where for the different interfaces $\dot{A}_{new}$ is shown versus different applied strain rates. From Figure 19 it can be concluded that the changed part of the interface is not confined to the region between the dislocation fragments in Fe and X. The structure change extends outside this region in the negative x-direction for the X1, X2, and X3

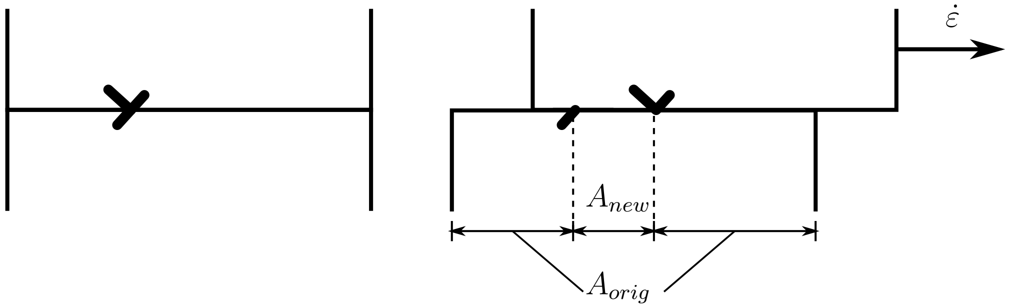

Figure 18: Schematic representation of structure change at the interface caused by sliding of the crystals. Once the upper crystal slides with respect to the lower crystal, the locations in the upper and lower crystal which were affected by the initial dislocation move apart, as is schematically illustrated by the two parts of the dislocation symbol. A_{new} and A_{orig} are the areas of the changed and original interface structures, $\dot{\varepsilon}$ determines the sliding velocity (110 Å/ns).

interface and in both positive and negative x-directions for the S2 interface. The rate of structure change shows a linear dependence on the strain rate, as indicated by the dashed curves in Figure 19 which are linear fits to the data. $\dot{A}_{new}$, however, is always larger than the sliding velocity and the dependence on the strain rate is interface and shear direction dependent.

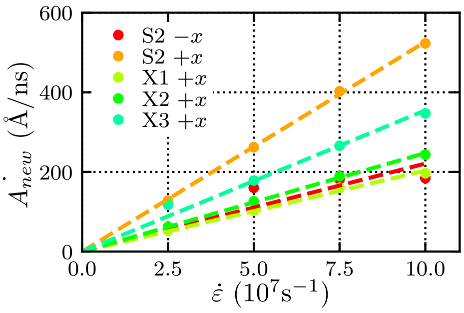

Figure 19: Rate of structure change versus applied strain rate for different interfaces. For all interfaces and strain rates the rate of structure change is larger than the sliding velocity. The dashed lines are linear fits to the data.

With the change rate as given in Figure 19 the overall tangential traction of the interface can be calculated with Equation 9 and compared with the actual obtained traction in the simulations as given in Section 3.2. This is illustrated for the S2 interface in Figure 20. As can be seen in Figure 20a, the cohesive law as given in Equation 9 is able to capture the increase in T_t caused by the changing interface structure. From Figure 20b it becomes clear, however, that for large separation T_t increases more than the cohesive law predicts. This is caused by the (artificial) periodicity of the simulation box. When the structure in a large part of the interface has changed, the stress in that part has increased. The unchanged part of the interface then feels the stress field from the changed region from both sides, due to the periodicity, leading to an increase in T_t in the unchanged part of the interface and therefore to an increase in the total T_t averaged over the interface.

In this study the focus is only on the interface behaviour during loading. If no structure change would occur at the interface, the unloading behaviour is expected to simply follow the cohesive law for the opposite shearing direction. However, as we have seen that the structure of the interface changes during loading, one cannot predict the behaviour during unloading with the current cohesive law and the parameters in Table B.2. Further study is necessary to capture the unloading behaviour in a cohesive law.

Only for interfaces which slide as rigid blocks without a dislocation, an influence of the dislocation on the shearing behaviour is seen. In this study only the influence of one dislocation of the $\{112\}\langle111\rangle$ slip system per interface is studied. Since the dislocation interacts with the interface under an angle, it can be expected that a different structure change would result for a dislocation of the same slip system but on a slip plane under a different angle with the interface, and therefore the interface behaviour would be different. Similarly, a dislocation of another slip system may cause a different structure change at the interface and therefore have a different influence on the shearing behaviour. With the current set-up of the simulations, it is not possible to study the effect of dislocations of the $\{110\}\langle111\rangle$ slip system on the interface behaviour for the interfaces in this study.

With the cohesive law derived in this section the traction-separation relations of different interfaces under a shear load can be implemented in larger-scale simulations.

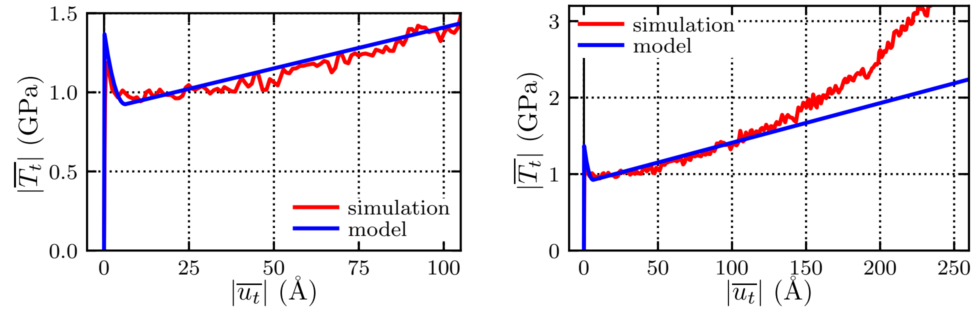

(a) (b)

Figure 20: T_t versus u_t for the S2 interface under shearing in the negative x-direction, as obtained from the simulations and as expressed by the fitted cohesive law, Equation 9. Note that panel (a) is an enlargement of panel (b).

5. Conclusions

From the response to a shear load of Fe – X bicrystals with 11 different interfaces we conclude that the interfaces can be divided into three different categories:

1. Interfaces along which the crystals slide as rigid blocks, with an equal behaviour of $T_t(u_t)$ for shearing in opposite directions, Section 3.1.1. These interfaces are found to be all those for which the energy of the most occurring realisation is also the minimum energy for the given crystal orientation relation. These are the interfaces S2, X1, and X3.
2. Interfaces along which the crystals slide following a gradual slip profile of the atoms in the upper atomic Fe planes, Section 3.1.2. These interfaces show a somewhat different behaviour of $T_t(u_t)$ for shearing in opposite directions. These are the interfaces Fe1, Fe3, Fe4, S1, S3, and S4.
3. Interfaces with mixed behaviour, i.e. with crystals sliding as rigid blocks in one direction and following a gradual slip profile of atoms in the upper Fe planes in the opposite direction, Section 3.1.3. These interfaces show a significantly different behaviour of $T_t(u_t)$ for the two opposite directions. These are the interfaces X2 and X4.

Considering only the interfaces from categories 2 and 3, and comparing only interfaces with one common crystal orientation, we conclude that, Section 3.1.4,

4. A lower interface energy leads to sliding at a higher tangential resistance.
5. The local atomic density at the interface does not determine the value of the sliding resistance.
6. A higher number of non-bcc Fe atoms at the interface leads to a higher sliding resistance.
7. There is no correlation between the number of non-bcc X atoms at the interface and the sliding resistance.
8. A stronger intermixing of Fe and X atoms across the interface, i.e. rougher surfaces at the interface, leads to a higher sliding resistance.

The influence of an initial dislocation in the Fe crystal just below the interface depends on the interface type:

9. For interfaces that slide following a gradual slip profile of the atoms in the upper atomic Fe planes two types of behaviour are observed, Section 3.2.1:

    - the dislocation completely dissolves in the interface and the overall response to a shear load is not modified,
    - the dislocation stays intact and the overall response to a shear load is not modified.

10. For interfaces that slide as rigid blocks two different types of behaviour are found:
    - the dislocation moves into the interface, triggers a structure change of the interface which makes it no longer possible for the crystals to slide as rigid blocks, and the overall response of the interface is significantly modified, Sections 3.2.3 and 3.2.2,
    - due to the sliding of the crystals the resolved shear stress does not increase enough for the dislocation to move into the interface, and the response of the interface is not modified, Section 3.2.3.

We derived a cohesive law to describe the relation between tangential traction and tangential separation at an interface during shearing.

11. The shear behaviour is described in three parts: an elastic part, a steady-state sliding part and a part in between, where the steady-state sliding behaviour develops.
12. This cohesive law is described by four parameters for every interface and for every loading direction.
13. The influence of a structure change of the interface triggered by the presence of a dislocation can be taken into account into this cohesive law by making it a linear combination of the original relation and the relation found for the changed structure, depending on the fraction of changed interface area. The rate of structure change is dependent on the interface, the shear direction and the strain rate.

6. Acknowledgement

This research was carried out under project number F22.2.13518b in the framework of the Partnership Program of the Materials Innovation Institute M2i and the Foundation of Fundamental Research on Matter (FOM), which is part of the Netherlands Organisation for Scientific Research (NWO). We are grateful to Erik van der Giessen and Tarun Katiyar for helpful discussions.

Appendix A. Behaviour of Fe3 interface under a shear load

As described in Section 3.1.2 the Fe3 interface shows a small difference for shearing in opposite directions. Apart from what was described in Section 3.1.2 there is another reason for this difference. When sheared to the right, as shown in Figure A.21(top), the Fe3 interface shows a decrease in average tangential traction. Shearing in both directions leads to a change in interface structure, with only a small difference in the number of non-bcc atoms Figure A.21(bottom). The resulting structures, however, are different, as shown in Figure A.22(top). When sheared to the right a wavy interface structure develops, while when sheared to the left the surfaces become rough. These different structures result in different atomic stresses along the interface, as can be clearly seen in Figure A.22(bottom), where stress concentrations corresponding to the wavy structure are shown. Since the different bins along the interface move through these stress concentrations at different moments in time, the standard deviation of the traction increases when the system is sheared to the right, Figure A.21(middle). The average tangential traction, as shown in Figure A.21(top), shows only a small deviation from the tangential traction that results when sheared to the left.

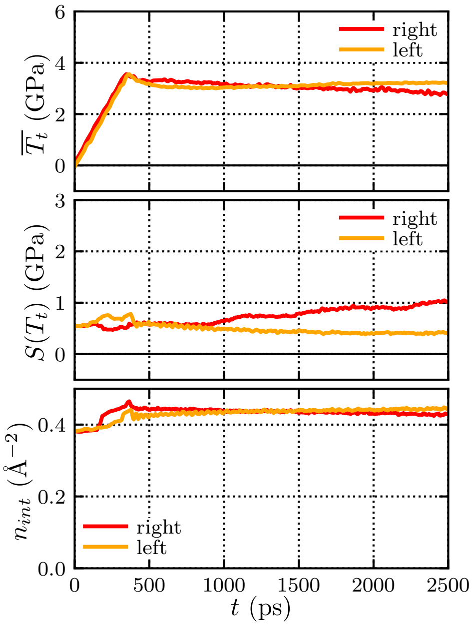

Figure A.21: Time evolution of the average (top) and standard deviation (middle) of the tangential traction in all bins and the number of non-bcc atoms per unit interface area (bottom) for the Fe3 interface (see Figure 3) under shear loading in opposite directions. To smoothen the curves the data points are averaged over 10 ps.

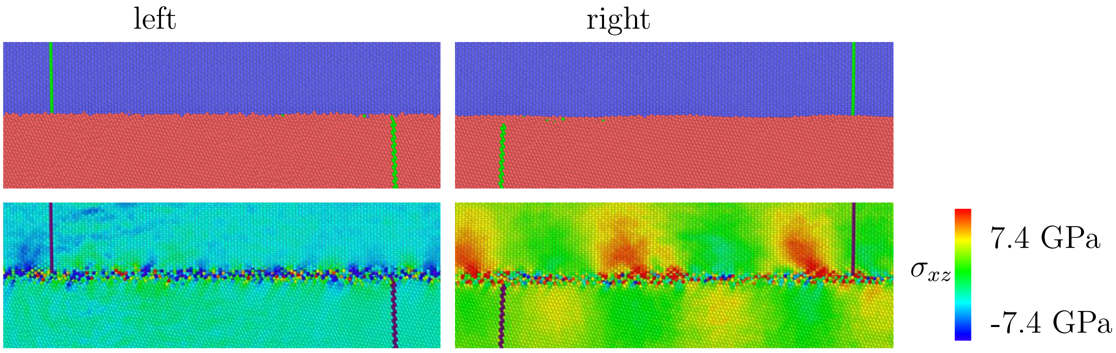

Figure A.22: Positions of Fe and X atoms (top) and stresses σ_{xz} (bottom) at the Fe3 interface after 2500 ps of shearing in the positive (right) and negative (left) x-directions. In the top panels atoms in blue are X, atoms in red are Fe. Atoms marked in green formed one vertical plane before shearing. In the lower panels this plane is marked in purple, and the other atoms are coloured according to σ_{xz}.

Appendix B. Parameters

Table B.2: Parameters for the cohesive law as given in Equation 7 describing the relation between T_t and u_t for all the studied interfaces. Values for u_t^{crit} and u_t^s are in Å, values for T_t^{crit} and T_t^s are in GPa.

	positive x-direction				negative x-direction			
Interface	u_t^{crit}	u_t^s	T_t^{crit}	T_t^s	u_t^{crit}	u_t^s	T_t^{crit}	T_t^s
Fe1	8.08	143.35	2.92	1.95	-3.75	-84.09	-2.64	-1.95
Fe3	2.36	132.67	3.56	2.99	-4.00	-20.91	-3.56	-3.15
Fe4	0.83	0.83	3.03	3.03	-1.49	-14.74	-3.70	-3.07
S1	0.69	82.26	0.86	0.34	-0.29	-0.29	-0.41	-0.41
S2	0.15	2.72	1.24	0.92	-0.14	-6.24	-1.37	-0.92
S3	3.72	5.16	2.71	2.47	-2.04	-28.92	-1.94	-2.80
S4	1.92	6.64	3.08	2.96	-1.58	-11.09	-3.57	-3.10
X1	0.14	0.14	0.02	0.02	-0.12	-0.12	-0.03	-0.03
X2	0.38	0.38	0.19	0.19	-1.78	-13.69	-2.47	-1.52
X3	0.00	0.00	0.01	0.01	0.00	0.00	-0.01	-0.01
X4	2.19	8.17	0.96	1.67	0.00	0.00	-0.06	-0.06

Data availability

The raw/processed data required to reproduce these findings cannot be shared at this time due to technical or time limitations.

References

[1] A. Elzas and B. J. Thijsse, “Cohesive law describing crack growth at iron/precipitate interfaces,” *Computational Materials Science*, vol. 134, pp. 214–224, 2017.

[2] G. I. Barenblatt, “The Mathematical Theory of Equilibrium Cracks in Brittle Fracture,” *Advances in Applied Mechanics*, vol. 7, pp. 55–129, 1962.

[3] D. Dugdale, “Yielding of steel sheets containing slits,” *Journal of the Mechanics and Physics of Solids*, vol. 8, no. 2, pp. 100–104, 1960.

[4] X. P. Xu and A. Needleman, “Void nucleation by inclusion debonding in a crystal matrix,” *Modelling and Simulation in Materials Science and Engineering*, vol. 1, no. 2, pp. 111–132, 1993.

[5] M. J. van den Bosch, P. J. G. Schreurs, and M. G. D. Geers, “An improved description of the exponential Xu and Needleman cohesive zone law for mixed-mode decohesion,” *Engineering Fracture Mechanics*, vol. 73, no. 9, pp. 1220–1234, 2006.

[6] J. Dollhofer, W. Beckert, B. Lauke, and K. Schneider, “Fracture mechanical characterisation of mixed-mode toughness of thermoplast/glass interfaces,” *Computational Materials Science*, vol. 19, no. 1-4, pp. 223–228, 2000.

[7] K. Park, G. H. Paulino, and J. R. Roesler, “A unified potential-based cohesive model of mixed-mode fracture,” *Journal of the Mechanics and Physics of Solids*, vol. 57, no. 6, pp. 891–908, 2009.

[8] J. P. McGarry, É. Ó. Máirtín, G. Parry, and G. E. Beltz, “Potential-based and non-potential-based cohesive zone formulations under mixed-mode separation and over-closure. Part I: Theoretical analysis,” *Journal of the Mechanics and Physics of Solids*, vol. 63, no. 1, pp. 336–362, 2014.

[9] R. Dimitri, M. Trullo, L. De Lorenzis, and G. Zavarise, “Coupled cohesive zone models for mixed-mode fracture: A comparative study,” *Engineering Fracture Mechanics*, vol. 148, pp. 145–179, 2015.

[10] X. W. Zhou, J. A. Zimmerman, E. D. Reedy Jr., and N. R. Moody, “Molecular dynamics simulation based cohesive surface representation of mixed mode fracture,” *Mechanics of Materials*, vol. 40, no. 10, pp. 832–845, 2008.

[11] X. W. Zhou, N. R. Moody, R. E. Jones, J. A. Zimmerman, and E. D. Reedy Jr., “Molecular-dynamics-based cohesive zone law for brittle interfacial fracture under mixed loading conditions: Effects of elastic constant mismatch,” *Acta Materialia*, 2009.

[12] D. E. Spearot, K. I. Jacob, and D. L. McDowell, “Non-local separation constitutive laws for interfaces and their relation to nanoscale simulations,” *Mechanics of Materials*, vol. 36, no. 9, pp. 825–847, 2004.

[13] D. E. Spearot, K. I. Jacob, D. L. McDowell, and S. J. Plimpton, “Effect of deformation path sequence on the behavior of nanoscale copper bicrystal interfaces,” *Journal of Engineering Materials and Technology*, vol. 127, no. 4, pp. 374–382, 2004.

[14] C. R. Dandekar and Y. C. Shin, “Molecular dynamics based cohesive zone law for describing Al-SiC interface mechanics,” *Composites Part A: Applied Science and Manufacturing*, vol. 42, no. 4, pp. 355–363, 2011.

[15] V. Yamakov, E. Saether, D. R. Phillips, and E. H. Glaessgen, “Molecular-dynamics simulation-based cohesive zone representation of intergranular fracture processes in aluminum,” *Journal of the Mechanics and Physics of Solids*, vol. 54, no. 9, pp. 1899–1928, 2006.

[16] V. Yamakov, E. Saether, and E. H. Glaessgen, “Multiscale modeling of intergranular fracture in aluminum: Constitutive relation for interface debonding,” *Journal of Materials Science*, vol. 43, no. 23-24, pp. 7488–7494, 2008.

[17] P. Gupta, S. Pal, and N. Yedla, “Molecular dynamics based cohesive zone modeling of Al (metal)-Cu50Zr50 (metallic glass) interfacial mechanical behavior and investigation of dissipative mechanisms,” *Materials & Design*, vol. 105, pp. 41–50, 2016.

[18] B. Paliwal and M. Cherkaoui, “An improved atomistic simulation based mixed-mode cohesive zone law considering non-planar crack growth,” *International Journal of Solids and Structures*, vol. 50, no. 20-21, pp. 3346–3360, 2013.

[19] G. J. Ackland, M. I. Mendelev, D. J. Srolovitz, S. Han, and A. V. Barashev, “Development of an interatomic potential for phosphorus impurities in α-iron,” *Journal of Physics: Condensed Matter*, vol. 16, no. 27, p. S2629, 2004.

[20] A. Elzas and B. J. Thijsse, "Dislocation impacts on iron/precipitate interfaces under shear loading," *Modelling and Simulation in Materials Science and Engineering*, vol. 24, no. 8, p. 85006, 2016.

[21] M. A. Tschopp and D. L. McDowell, "Structures and energies of Σ 3 asymmetric tilt grain boundaries in copper and aluminium," *Philosophical Magazine*, vol. 87, no. 22, pp. 3147–3173, 2007.

[22] "LAMMPS Molecular Dynamics Simulator." `http://lammps.sandia.gov`.

[23] A. Pineau, "Fast Parallel Algorithms for Short-Range Molecular Dynamics," *Journal of Computational Physics*, vol. 117, no. 1, pp. 1–19, 1995.

[24] W. M. Brown, P. Wang, S. J. Plimpton, and A. N. Tharrington, "Implementing Molecular Dynamics on Hybrid High Performance Computers - Short Range Forces," *Computer Physics Communications*, vol. 182, pp. 898–911, 2011.

[25] W. M. Brown, A. Kohlmeyer, S. J. Plimpton, and A. N. Tharrington, "Implementing Molecular Dynamics on Hybrid High Performance Computers - Particle-Particle Particle-Mesh," *Computer Physics Communications*, vol. 183, pp. 449–459, 2012.

[26] W. M. Brown and Y. Masako, "Implementing molecular dynamics on hybrid high performance computers Three-body potentials," *Computer Physics Communications*, vol. 184, pp. 2785–2793, 2013.

[27] A. Stukowski, "Visualization and analysis of atomistic simulation data with OVITO–the Open Visualization Tool," *Modelling Simul. Mater. Sci. Eng.*, vol. 18, no. 1, p. 015012, 2009.

[28] D. Faken and H. Jónsson, "Systematic analysis of local atomic structure combined with 3D computer graphics," *Computational Materials Science*, vol. 2, no. 2, pp. 279–286, 1994.

[29] H. Tsuzuki, P. S. Branicio, and J. P. Rino, "Structural characterization of deformed crystals by analysis of common atomic neighborhood," *Computer Physics Communications*, vol. 177, pp. 518–523, sep 2007.